Nature Communications

https://doi.org/10.1038/s41467-026-72161-w

Article in Press

Temporal heterogeneity shapes diffusion dynamics in complex networks

Received: 24 November 2025

Accepted: 8 April 2026

Cite this article as: Luo, C., Lambiotte, R., Ji, P. Temporal heterogeneity shapes diffusion dynamics in complex networks. *Nat Commun* (2026). https://doi.org/10.1038/s41467-026-72161-w

Cheng Luo 成, Renaud Lambiotte & Peng Ji

Temporal heterogeneity shapes diffusion dynamics in complex networks

Cheng Luo (罗成)[1,2], Renaud Lambiotte[3], Peng Ji (纪鹏)[1,2,4*]

[1*]Interdisciplinary Research Centre for Complex Systems, Institute of Science and Technology for Brain-Inspired Intelligence, Fudan University, Shanghai, 200433, China.
[2]Key Laboratory of Computational Neuroscience and Brain-Inspired Intelligence, Ministry of Education, Shanghai, 200433, China.
[3]Mathematical Institute, University of Oxford, Woodstock Road, Oxford, OX2 6GG, United Kingdom.
[4]MOE Frontiers Center for Brain Science, Fudan University, Shanghai, 200433, China.

*Corresponding author(s). E-mail(s): pengji@fudan.edu.cn;

Abstract

Network diffusion underpins diverse phenomena from social contagion to neural dynamics, yet real-world spreading processes often exhibit complex temporal heterogeneity that transcends Markovian assumptions. Here we present a general theoretical framework incorporating node-specific waiting-time distributions through renewal processes, enabling the integration of temporal heterogeneity with network topology. By formulating dynamics in the Laplace domain, we derive closed-form expressions linking local temporal statistics to the network's spectral properties, yielding analytical bounds on relaxation times, mixing behavior, and sensitivity to temporal perturbations. Our approach provides quantitative criteria predicting how local timing alterations propagate to global dynamics. We validate the framework through numerical experiments and empirical analysis of $\boldsymbol{\alpha}$-synuclein spreading in mouse brain networks, where Gamma-based temporal kernels significantly outperform memoryless models. This work establishes a unified foundation for studying non-Markovian diffusion, with implications for understanding spreading processes across biological and social systems.

Introduction

Diffusion in complex systems is a fundamental process underlying diverse phenomena—from rumor and epidemic spreading in social networks [1] to neuronal firing and neurodegenerative progression in the brain [2], and cascading failures in power grids [3]. Both network topology and various forms of nonlinear dynamical interactions shape the pattern and evolution of diffusion [4]. While traditional models often rely on pairwise interactions, recent studies reveal that higher-order interactions can substantially alter diffusion dynamics—for instance, by reducing the size of attraction basins of ordered states, increasing their multiplicity, and inducing abrupt phase transitions [5–8]. Moreover, the interplay between topology and nonlinear dynamics can further amplify the complexity of diffusion [9]. A deeper understanding of this relationship is therefore essential for characterizing diffusion in real-world systems.

Markov models have served as a powerful framework for illustrating diverse diffusion patterns and their evolution. When the process is memoryless under the first-order Markov assumption, it reduces to a random walk on a graph. However, empirical evidence increasingly highlights the importance of memory effects in information and epidemic spreading [10, 11]. Although higher-order Markov chains capture structural memory in state transitions, they often fail to represent temporal memory arising from non-Poissonian inter-event time statistics—commonly observed in systems ranging from human activity to neural dynamics [9, 12, 13]. Such temporally heterogeneous, non-Markovian dynamics can be naturally modeled using renewal processes, where each node follows a general waiting-time distribution [14, 15].

In this work, we focus on a non-Markovian model with heterogeneous waiting-time distributions across nodes, emphasizing renewal processes as a key generalization of the Poisson process. By allowing arbitrary inter-event time distributions, renewal processes offer a natural and powerful framework for capturing the heterogeneous temporal patterns observed in real-world diffusion [16]. Yet, critical gaps persist in applying them to networked systems. Most existing studies rely on homogeneity assumptions or numerical simulations, leaving a central question open [17, 18]: how does node-level temporal heterogeneity shape the global dynamics of diffusion?

To address this, we develop a general framework for analyzing network diffusion with arbitrary inter-event time distributions, aiming to clarify how temporal heterogeneity interacts with network structure to shape collective dynamics. By formulating the dynamics in the Laplace domain, we derive explicit expressions that connect waiting-time statistics with spectral properties, enabling the analysis of mixing and transient behaviors beyond Markovian descriptions. This approach also offers a principled way to quantify how global dynamics respond to local temporal perturbations, leading naturally to a measure of nodes' dynamical importance in renewal-driven diffusion [19, 20]. Although such node-level measures yield practical insights—with applications from brain network vulnerability [21–23] to influence maximization [24, 25]—they arise here as part of a broader goal: to establish a unified methodological foundation for studying non-Markovian diffusion in complex networks.

Results

We analyze a continuous-time random walk on networks, a fundamental model for non-Markovian diffusion. At each step, a walker at node i randomly selects an adjacent node j according to an $n \times n$ transition matrix $\boldsymbol{P}$, where P_{ij} denotes the transition probability from i to j (with $\sum_j P_{ij} = 1$ so that $\boldsymbol{P}$ is row-stochastic, and $P_{ii} = 0$ so that self-loops are excluded). Unlike discrete-time random walks, the inter-event times between jumps follow node-specific waiting time distributions $\rho_i(t)$. The dynamics are fully characterized by the conditional probability $X_{ij}(t)$ (the component giving the probability that a walker starting at node i occupies node j at time t), which satisfies the generalized master equation [15]

$$X_{ij}(t) = \delta_{ij} \int_t^\infty \rho_i(\tau)\, d\tau \; + \; \int_0^t \sum_{k \neq i} \rho_i(\tau)\, P_{ik}\, X_{kj}(t-\tau)\, d\tau, \tag{1}$$

where δ_{ij} is the Kronecker delta and we write $\boldsymbol{\rho}(t) = \mathrm{diag}\{\rho_1(t), \ldots, \rho_n(t)\}$ for the diagonal matrix of waiting-time densities. The first term represents persistence at the initial node i, while the second term accounts for probability flow through network jumps. The initial condition for the process is $X_{ij}(0) = \delta_{ij}$, consistent with the interpretation of $X_{ij}(t)$. For notational convenience we will also use the matrix notation $\boldsymbol{X}(t)$ to denote the $n \times n$ matrix whose (i, j) entry is $X_{ij}(t)$; by construction, $\boldsymbol{X}(t)$ is a row-stochastic matrix for all t. The transpose formulation yields a dual consensus process where $X_{ij}(t)$ represents the value at node i given initial conditions at node j. For connected undirected networks, this dynamics asymptotically converges to uniform consensus ($X_{ij} = X_{lj}$ for all i, j, l).

The master equation (1) reveals the non-Markovian nature of the process through its history-dependent integral term, while showing a dependence on both network structure (via $\boldsymbol{P}$) and the temporal dynamics (via $\boldsymbol{\rho}(t)$). These features collectively determine the diffusion rate of the system. For exponential waiting times $\rho_i(t) = \mu_i^{-1} \exp(-t/\mu_i)$, the system becomes Markovian, reducing to the differential equation

$$\frac{\mathrm{d}}{\mathrm{d}t}\boldsymbol{X}(t) = \mathrm{diag}\{\mu_1^{-1}, \ldots, \mu_n^{-1}\}(\boldsymbol{P} - \boldsymbol{I})\boldsymbol{X}(t), \tag{2}$$

where μ_i is the mean waiting time at node i. This memoryless approximation has successfully modeled diffusion processes in a range of applications [4]. In neuropathological diffusion, which we will investigate at the end of this work, applications include dementia progression [21], α-synuclein spread [22], and τ propagation [23].

The relaxation dynamics of the system are characterized by the timescales τ_{ij}, defined as the supremum of all $a > 0$ for which the integral $\tau_{ij} = \sup\{a | \int_0^\infty \exp(t/a)(X_{ij}(t) - X_{ij}(\infty))dt\}$ converges. The mixing time $\tau_{\mathrm{mix}} \equiv \max_{i,j} \tau_{ij}$ determines the slowest mode of asymptotic convergence to equilibrium and is, importantly, independent of initial conditions in our framework. To characterize the asymptotic convergence while avoiding the influence of stationary states $\boldsymbol{X}(\infty)$, we define $\boldsymbol{Y}(t) = \boldsymbol{X}(t) - \boldsymbol{X}(\infty)$. Through Laplace transformation of the master equation,

we obtain the spectral representation

$$\hat{\boldsymbol{Y}}(s) = s^{-1}\left[(\boldsymbol{I} - \hat{\boldsymbol{\rho}}(s)\boldsymbol{P})^{-1}(\boldsymbol{I} - \hat{\boldsymbol{\rho}}(s)) - \boldsymbol{X}(\infty)\right], \tag{3}$$

where $\hat{\boldsymbol{Y}}(s)$ is the Laplace transform of $\boldsymbol{Y}(t)$, and $\hat{\boldsymbol{\rho}}(s) = \int_0^\infty e^{-st}\boldsymbol{\rho}(t)\mathrm{d}t$ is that of the waiting time distribution matrix. The poles of $\hat{\boldsymbol{Y}}(s)$ provide crucial insights into the system's relaxation behavior. Each relaxation rate is associated to a pole at $-1/\tau_{ij}$ with negative real part, and the mixing time τ_{mix} is determined by the pole closest to the imaginary axis. This pole structure emerges from two fundamental components: the transform of the memory kernel $\hat{\boldsymbol{\rho}}(s)$ encoding temporal correlations, and the network propagator $(\boldsymbol{I} - \hat{\boldsymbol{\rho}}(s)\boldsymbol{P})^{-1}$ capturing topological influences.

For the form of the waiting time distributions, motivated by empirical observations [13], we consider $\rho_i(t) = \rho_i^0(t)\exp(-t/\tau_{\text{tail}}^i)$, where $\rho_i^0(t)$ is a fat-tailed distribution, i.e. whose tail decreases slower than an exponential for large values of t, and where $\exp(-t/\tau_{\text{tail}}^i)$ ensures an exponential decay for the asymptotics of the distribution. Consequently, for the first term of (3), each τ_{tail}^i is a pole of $\hat{\boldsymbol{Y}}(s)$, and $\hat{\boldsymbol{Y}}(s)$ is well defined only when $s > \max\{-1/\tau_{\text{tail}}^i\}$. For the second term, defining $\hat{\boldsymbol{Q}}(s) = \boldsymbol{I} - \hat{\boldsymbol{\rho}}(s)\boldsymbol{P}$, it can be shown that a pole of $\hat{\boldsymbol{Q}}(s)^{-1}$ is equivalent to a root of $|\hat{\boldsymbol{Q}}(s)| = 0$ (see Supplementary Note 2.5 for details), thus requiring us to solve

$$|\boldsymbol{I_n} - \mathrm{diag}\{\hat{\rho}_1(s), \cdots, \hat{\rho}_n(s)\}\boldsymbol{P}| = 0. \tag{4}$$

We denote the largest negative real part of the roots as s_{mix}, so that $\tau_{\text{mix}} = -1/s_{\text{mix}}$.

The homogeneous case with identical waiting time distributions at all nodes, $\rho_i(t) = \rho(t) = \rho^0(t)\exp(-t/\tau_{\text{tail}})$, admits an exact solution [9]. Considering the eigenvalues of the transition matrix $1 = \lambda_0(\boldsymbol{P}) > \lambda_1(\boldsymbol{P}) \geq \cdots \geq \lambda_{n-1}(\boldsymbol{P}) \geq -1$, and $|\boldsymbol{Q}(s)| = \prod_{i=0}^{n-1}(1 - \lambda_i\hat{\rho}(s))$, we obtain $\tau_{mix} = -1/\hat{\rho}^{-1}(1/\lambda_1(\boldsymbol{P}))$.

To obtain a closed-form estimate, we approximate $\hat{\rho}(s)$ by its $(1,1)$ Padé form. This approximation captures both the mean and variance of the waiting-time distribution, while maintaining the algebraic simplicity required for an explicit solution of the root condition. Physically, the inverse Laplace transform of the $(1,1)$ Padé form approximates the waiting-time distribution as a mixture of an exponential decay and a Dirac delta distribution, effectively characterizing both the average waiting time and the impact of temporal heterogeneity (i.e., long-tail effects). With this Padé approximation, one obtains the explicit expression

$$\tau_{\text{mix}} \approx \max\{\frac{\mu}{1 - \lambda_1(\boldsymbol{P})} + \frac{\sigma^2 - \mu^2}{2\mu}, \tau_{\text{tail}}\}, \tag{5}$$

where μ and σ^2 represent the mean and variance of the waiting time distribution, respectively. This result demonstrates that the asymptotic dynamics depends crucially on the network structure through the spectral gap $1 - \lambda_1(\boldsymbol{P})$, and the temporal statistics via μ, σ^2, and τ_{tail}. The competition between these factors determines the dominant timescale of the system.

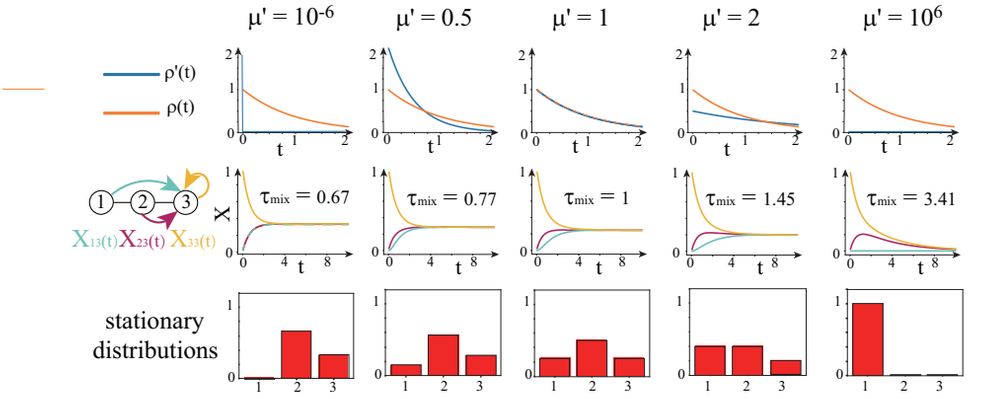

Fig. 1 Mixing time analysis for a 3-node linear network where node 1 has variable transition rate $\mu' \in \{10^{-6}, 0.5, 1, 2, 10^6\}$, while nodes 2–3 maintain $\mu = 1$. The dynamics follow Eq. (2), revealing how modifying μ' values affects both mixing times and asymptotic states.

The heterogeneous case with non-uniform waiting time distributions across nodes presents significant analytical challenges. We focus here on a minimal perturbation scenario where a single node (node k) has a modified distribution $\rho'(t)$ with mean μ' and tail parameter τ'_{tail}, while all other nodes share the same baseline distribution $\rho(t)$. This setup, which can be interpreted as a targeted modification of the waiting time on a specific node, allows us to systematically investigate how local modifications to temporal dynamics affect the global mixing time τ_{mix}.

As an illustration, we consider the generalized master equation (1) on a simple 3-node linear network (Fig. 1). Initially, all nodes have identical exponential waiting-time distributions with rate $\mu = 1$, but we vary μ' for node 1, a system that can be investigated by the differential equation (2). For the unmodified case ($\mu' = 1$), the system's convergence rate gives a mixing time $\tau_{\text{mix}} = 1$. When μ' increases (e.g., $\mu' = 2$ or $\mu' = 10^6$), node 1 tends to absorb the random walkers, leading to a larger τ_{mix}. Conversely, when μ' decreases, e.g., $\mu' = 0.5$ or $\mu' = 10^{-6}$, node 1 essentially acts as a transient state, accelerating convergence and shortening τ_{mix}. As we will see, the range of responses resulting from the modification of node 1's waiting time depends on the network structure and dynamics and can serve as a way to identify the centrality of nodes in a temporal network.

Going back at the more general case of a non-exponential distribution, the mixing time τ'_{mix} can be found by looking at the spectral properties of the $(n-1) \times (n-1)$ cofactor matrix $\boldsymbol{M}_{kk}$ of the element $\boldsymbol{P}_{kk}$ (see Supplementary Note 3.3), and is analytically determined by the root of $|\hat{\boldsymbol{Q}}(s)| = 0$, specifically through the eigenvalues of $\boldsymbol{P}$ and $\boldsymbol{M}_{kk}$:

$$\frac{\hat{\rho}(s)}{\hat{\rho}'(s)} = 1 - \frac{\prod_{i=0}^{n-1}(1 - \lambda_i(\boldsymbol{P})\hat{\rho}(s))}{\prod_{i=1}^{n-1}(1 - \lambda_i(\boldsymbol{M}_{kk})\hat{\rho}(s))}, \tag{6}$$

where the $n-1$ eigenvalues of $\boldsymbol{M}_{kk}$ verify $\lambda_{n-1}(\boldsymbol{P}) \leq \lambda_{n-1}(\boldsymbol{M}_{kk}) \leq \cdots \leq \lambda_1(\boldsymbol{P}) \leq \lambda_1(\boldsymbol{M}_{kk}) \leq \lambda_0(\boldsymbol{P})$. While numerical computation of mixing times is computationally expensive, our analytical solution in Eq. (6) provides an accurate and efficient alternative, reducing computational costs by several orders of magnitude while maintaining

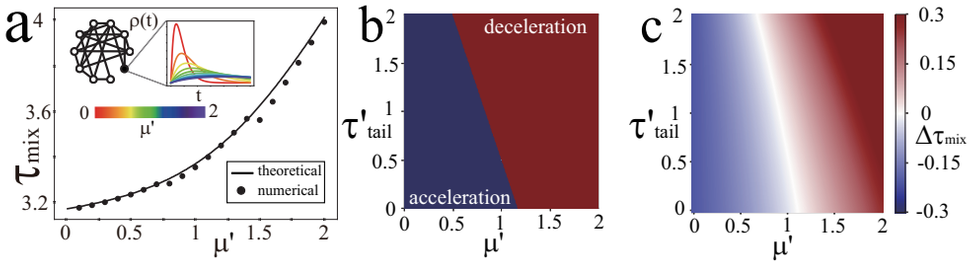

Fig. 2 Comparison of theoretical predictions and numerical results for convergence modifications. (a-c) Numerical validation on Erdős–Rényi (ER) networks (10 nodes, 20 edges) with Gamma-distributed waiting times ($\mu = 1$, $\tau_{\text{tail}} = 0.5$) for all nodes except one target node. (a) Comparison between theoretical predictions (6) and simulations for $\mu' = 2\tau'_{\text{tail}}$ ($\mu' \in (0, 2)$). (b) Theoretical $\Delta\tau_{\text{mix}}$ (8) heatmap across $(\tau'_{\text{tail}}, \mu')$ parameter space. (c) Corresponding numerical convergence results.

high precision. To demonstrate this, we simulate the generalized master equation (1). All nodes initially follow identical Erlang distributions (a special Gamma distribution) with $\mu = 2\tau_{\text{tail}} = 1$. We then modify a randomly selected node's waiting-time distribution by varying $\mu' = 2\tau'_{\text{tail}}$ within the interval $(0, 2)$. Fig. 2a shows excellent agreement between our theoretical predictions of τ_{mix} and numerical simulations.

To proceed further with our analytical investigation, we start with a qualitative analysis on the case where the waiting time distributions follow Gamma distributions, defined as

$$\rho(t) = \frac{t^{\mu/\tau_{\text{tail}}-1}}{\Gamma(\mu/\tau_{\text{tail}})\tau_{\text{tail}}^{\mu/\tau_{\text{tail}}}} e^{-t/\tau_{\text{tail}}}, \tag{7}$$

with the parameters modified to μ' and τ'_{tail} for the target node. Applying the (1,1) Padé approximation to $\hat{\rho}(s)$ and $\hat{\rho}'(s)$, we find (see Supplementary Note 3.4) that the change of mixing time $\Delta\tau_{\text{mix}} = \tau'_{\text{mix}} - \tau_{\text{mix}}$ verifies

$$\begin{aligned}\text{sign}(\Delta\tau_{\text{mix}}) \approx \text{sign}\,((\tau'_{\text{tail}} - \tau_{\text{tail}})(1 - \lambda_1(\boldsymbol{P})) \\ +(\mu' - \mu)(1 + \lambda_1(\boldsymbol{P}))\,.\end{aligned} \tag{8}$$

The convergence dynamics are quantitatively characterized by $\Delta\tau_{\text{mix}}$, where negative values indicate accelerated relaxation ($\tau'_{\text{mix}} < \tau_{\text{mix}}$) and positive values correspond to deceleration ($\tau'_{\text{mix}} > \tau_{\text{mix}}$). Interestingly, whether the process is accelerated or decelerated does not depend on the choice of node k. Instead, it depends solely on the spectral gap $\lambda_1(\boldsymbol{P})$ and the parameters of the two waiting time distributions. Larger values of $\lambda_1(\boldsymbol{P})$, indicating a stronger community structure of the network, give more importance to the mean of the distribution over its exponential tail. Fig. 2b presents the theoretical predictions of the convergence of the asymptotic state from (8) through a $\Delta\tau_{\text{mix}}$ heatmap across the $(\tau'_{\text{tail}}, \mu')$ parameter space, while Fig. 2c shows the corresponding numerical convergence results.

To explore the amplitude of $\Delta\tau_{\text{mix}}$ in the case of a general distribution, not necessarily Gamma, we consider two extreme cases, defining an upper and a lower bound for the mixing time. We first consider the case where the waiting time at node k is

extremely slow, such that $\tau'_{\text{tail}} \to \infty$ and $\mu' \to \infty$. In this case, Eq. (4) can be rewritten as

$$|\text{diag}\{1/\hat{\rho}_1(s), \cdots, 0, \cdots, 1/\hat{\rho}_n(s)\} - \boldsymbol{P}| = 0. \tag{9}$$

This corresponds to a scenario where node k acts as an absorbing state, and the average residence time of the walker at node k tends to infinity. By solving Eq. (9), we can obtain the mixing time τ'_{mix}. Further, when the waiting time distributions for all nodes, except node k, are identical, we can derive the upper bound for $\Delta\tau_{\text{mix}}$(see Supplementary Note 4.2 for details)

$$\Delta\tau_{\text{mix}} = \frac{-1}{\hat{\rho}^{-1}(1/\lambda_1(\boldsymbol{M}_{kk}))} + \frac{1}{\hat{\rho}^{-1}(1/\lambda_1(\boldsymbol{P}))}. \tag{10}$$

This expression captures the time needed for the entire probability mass to be absorbed by the target node k, combining both dynamical and structural properties to serve as a dynamical centrality.

To obtain a tractable degree-based approximation of the upper bound, we next estimate $\lambda_1(\mathbf{M}_{kk})$ using a heterogeneous mean-field approach within the configuration model. The configuration model is a widely used random-graph null model that randomizes edges while controlling for degree information. Here we consider the degree-sequence ensemble, where the degree sequence is fixed and edges are otherwise wired uniformly at random; it therefore retains degree heterogeneity but averages out higher-order correlations [26]. Within this framework one obtains a simple leading-order estimate, valid when the leading eigenvalue is close to unity (see Supplementary Note 4.4 for details), $\lambda_1(\mathbf{M}_{kk}) \approx \frac{\sum_i d_i - d_k}{\sum_i d_i} = 1 - \frac{d_k}{2m}$, where d_i denotes the degree of node i and m is the number of edges. In this case, the upper bound (10) can be further approximated as

$$\Delta\tau_{\text{mix}} \approx \mu\left(\frac{2m}{d_k} - 1\right) + \frac{1}{\hat{\rho}^{-1}(1/\lambda_1(\boldsymbol{P}))}. \tag{11}$$

This implies that the combination of the dynamical property μ and the local structure d_k can determine the change of the mixing time $\Delta\tau_{\text{mix}}$.

For the other case where the waiting time on node k becomes extremely short, such that $\tau'_{\text{tail}} \to 0$ and $\mu' \to 0$, Eq. (4) can be rewritten as

$$|\text{diag}\{1/\hat{\rho}_1(s), \cdots, 1, \cdots, 1/\hat{\rho}_n(s)\} - \boldsymbol{P}| = 0. \tag{12}$$

This corresponds to the scenario where the average residence time of the walker at node k tends to 0. In this case, we can derive the lower bound as

$$\Delta\tau_{\text{mix}} = \frac{-1}{\hat{\rho}^{-1}(1/\lambda_1(\boldsymbol{M}_{kk} + \boldsymbol{P}_{k\cdot} \cdot \boldsymbol{P}_{\cdot k}^T))} + \frac{1}{\hat{\rho}^{-1}(1/\lambda_1(\boldsymbol{P}))}, \tag{13}$$

where $\boldsymbol{P}_{k\cdot}$ and $\boldsymbol{P}_{\cdot k}$ are obtained as $(n-1)$-dimensional vectors by removing $\boldsymbol{P}_{k,k}$ from the $k-$th row and column of $\boldsymbol{P}$, respectively. In the configuration model, $\boldsymbol{P}_{k\cdot} \cdot \boldsymbol{P}_{\cdot k}^T \to 0$, and it can be proven through block matrix eigenvalue analysis that $\lambda_2(\boldsymbol{M}_{kk}) \approx \lambda_1(\boldsymbol{P})$. According to the Bauer-fike theorem, one can further prove that $\lambda_2(\boldsymbol{M}_{kk}) \approx \lambda_1(\boldsymbol{M}_{kk} + \boldsymbol{P}_{k\cdot} \cdot \boldsymbol{P}_{\cdot k}^T)$, leading to the approximation of the lower bound $\Delta\tau_{\text{mix}} \approx 0$.

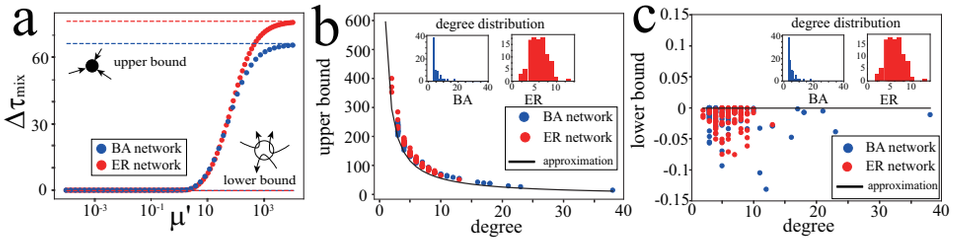

Fig. 3 Upper and lower bounds approximation in general network structures. (a) Monotonic growth of $\Delta\tau_{\text{mix}}$ with μ', bounded by (10) and (13). (b) Validation of degree-based approximation (11) against theoretical upper bound (10). (c) Asymptotic convergence of (13) to zero. Here, we numerically investigate the exponential waiting-time networks ($\mu = 1$ for all nodes except a target node) on ER and BA networks (100 nodes, 300 edges). The target node's waiting-time parameter μ' varies in $(0, 2)$.

Although the bounds (11) and (13) for $\Delta\tau_{\text{mix}}$ were derived under the configuration-model assumption, our numerical simulations demonstrate their validity in both ER random and BA scale-free networks. We consider exponentially distributed waiting times with $\mu = 1$ for all nodes, except for a target node with modified parameters μ' following $\rho'(t) = \mu'^{-1}\exp(-t/\mu')$, where $\mu' \in (0, 2)$. The mixing times τ'_{mix} computed via (6) show that $\Delta\tau_{\text{mix}}$ increases with μ', while remaining bounded between (10) and (13) (Fig. 3a). These results, obtained for randomly selected targets, suggest that $\Delta\tau_{\text{mix}}$ may characterize nodes' dynamical centrality.

To explore this further, we compute the bounds of $\Delta\tau_{\text{mix}}$ across all nodes and project them against node degree to reveal their topological dependence. Fig. 3b demonstrates strong agreement between the theoretical upper bounds (10) and their degree-based approximations (11). Notably, Fig. 3c shows that the lower bounds (13) effectively vanish network-wide, consistent with the analytical prediction that they provide only a negligible constraint in this regime. Overall, the upper bounds exhibit a clear negative correlation with node degree, while the lower bounds remain degree-independent and approach zero.

The reliability of the configuration-model-based approximations in these simulations is further supported by additional analytical and numerical evidence (see Supplementary Note 4.4–4.6 for details). In particular, the degree-dependent estimate for $\lambda_1(\mathbf{M}_{kk})$ can be derived and its leading correction terms can be identified by accounting for degree heterogeneity and finite-size effects. Consistent with this analysis, a systematic network-size scan on ER and BA network ensembles at $\langle k\rangle = 6$ shows that the mean node-level relative error of the $\lambda_1(\mathbf{M}_{kk})$ approximation decreases with increasing N and is already of order 10^{-3} for $N = 100$. By contrast, the corresponding approximation for $\Delta\tau_{\text{mix}}$ does not inherit the same monotone N-dependence, because mapping λ_1 to $\Delta\tau_{\text{mix}}$ involves the nonlinear transformation $1/(1-\lambda_1)$; accordingly, the mean relative error in $\Delta\tau_{\text{mix}}$ increases from small N but changes only weakly once N is sufficiently large. For the parameter regime used in Fig. 3b, this yields a moderate mean relative error for $\Delta\tau_{\text{mix}}$ of approximately 16%–19%.

We also assess the sensitivity of these approximations to triangle-induced correlations by varying clustering through degree-preserving rewiring and measuring the errors as a function of the global clustering coefficient (global transitivity) C. In the

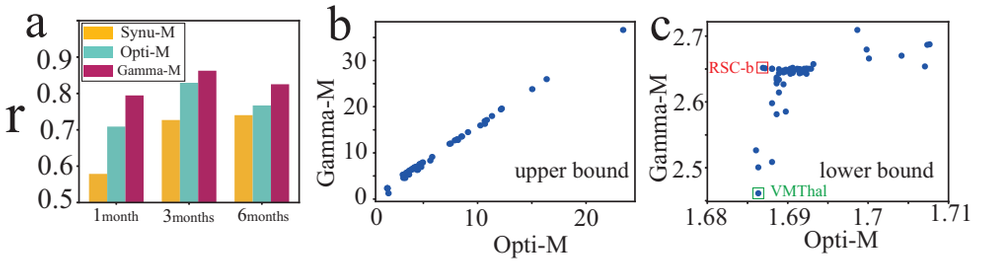

Fig. 4 Comparative analysis of pathological protein spread models in post-injection mouse brains. (a) Model-observation agreement for three propagation models (Synu-M, Opti-M, Gamma-M) shown through Pearson correlations (r) of log-transformed pathology densities across brain regions at 1, 3, and 6 months post-injection. (b) Theoretical upper bounds on mixing times from Eq. (9), comparing the Opti-M and Gamma-M models. (c) Corresponding lower bounds from Eq. (12) comparison between both models. Data are available in [22].

ER and BA networks used in our simulations before rewiring, clustering is typically below 0.1. Over this baseline-to-moderate range, the eigenvalue approximation error increases only gradually as C is raised, and the corresponding $\Delta\tau_{\text{mix}}$ error follows the same qualitative trend: for $C < 0.4$ the mean errors remain controlled and grow slowly with clustering. When rewiring drives the networks to larger clustering ($C > 0.4$), both errors rise rapidly, indicating a clear loss of accuracy once triangle-induced correlations become strong. Taken together, these results delineate the clustering regime in which the configuration-model baseline captures the leading, degree-driven contribution for the simulations considered in Fig. 3b, and they clarify how the approximation degrades when C is pushed far beyond the baseline networks.

To illustrate the potential applications of our findings in an empirical setting, we consider the mapping of spatiotemporal α-synuclein pathology patterns in the brain [22], typically modeled with a exponential waiting-time distribution assumption, leading to diffusion equations similar to Eq. (2). Specifically, we first establish a baseline model, Synu-M, which replicates the experimental setting in Ref. [22]. This model assumes that α-synuclein pathogenicity depends on regional endogenous mRNA expression levels. We incorporate this by modulating the parameters of the waiting-time distributions across regions, where the mean waiting times μ_i are determined by the inverse of the local mRNA concentrations weighted by the row sums of the structural connectivity matrix. This formulation accounts for the non-normalized nature of the connectome and implies a subtle influence of gene expression: rather than a simple direct inverse proportionality, mRNA levels modulate the effective spreading rates in conjunction with the regional structural connection strength, thereby shaping the overall temporal heterogeneity of the system. The network structure itself is maintained through the transition matrix $\boldsymbol{P}$, derived from retrograde viral tract tracing.

Our simulations reveal agreement between predicted and observed pathology, with Pearson correlations (r) reaching ≈ 0.7 for log-transformed values across all brain regions (Fig. 4a). Optimization of the diagonal matrix elements (Opti-M) yields progressive improvement in predictive accuracy versus Synu-M: the correlation increases from 0.58 to 0.71 at 1 month, 0.72 to 0.83 at 3 months, and 0.72 to 0.78 at 6 months (Fig. 4a), demonstrating robust capture of neuropathological progression dynamics.

While the exponential model (2) has the advantage of simplicity, its memorylessness may not be physiologically plausible and may limit its predictive accuracy. Considering the $n = 116$ brain regions involved, we exploit left–right structural and functional symmetry by tying mirror regions to identical parameters, thereby reducing the effective number of free parameters. These parameters are optimized to maximize the average Pearson correlation across 1, 3, and 6 months post-injection. Consequently, Opti-M involves fitting 58 independent mean parameters μ_i, while Gamma-M denotes the corresponding gamma waiting-time model, which assumes gamma-distributed waiting times, and requires 116 parameters (optimizing both mean and exponential tail per symmetric region). Gamma-M delivers superior performance, achieving $r > 0.79$ across all age groups (Fig. 4a) and a 15% improvement in goodness-of-fit over the exponential-based model, confirming both enhanced precision and broader applicability.

Through analysis of extreme cases using Eqns. (9) and (12), we establish region-specific bounds. Although both Opti-M and Gamma-M exhibit comparable upper bounds (Fig. 4b) and their lower bounds converge to similar values, analysis of the lower bounds reveals model-dependent variations in the implied dynamical centrality across brain regions (Fig. 4c). A representative example is provided by regions VMThal and RSC-b: whereas Opti-M yields identical centrality values (1.685), Gamma-M produces moderately different estimates (2.45 vs. 2.65), illustrating how the choice of waiting-time parametrization can influence the model's internal ranking of regions rather than indicating a definitive biological distinction.

Discussion

Understanding how temporal statistics shape transport on networks is central to building models that remain faithful to the heterogeneous timing patterns observed in real systems. Classical Poisson-based diffusion models offer analytical clarity but rely on a memoryless assumption that seldom holds empirically. Burstiness, heavy tails, and other forms of temporal heterogeneity can substantially reshape both transient behaviour and long-time relaxation, often in ways inaccessible to Markovian dynamics. The framework developed here addresses this challenge by modelling diffusion as a renewal-driven process and by deriving analytic tools that link non-exponential waiting-time distributions to the spectral properties of the underlying network.

Our perspective is primarily methodological. Rather than beginning from node-level constructs such as centrality, we formulate a general framework for non-Markovian diffusion in which arbitrary waiting-time kernels can be incorporated and analysed systematically. The Laplace-domain description separates temporal and structural contributions, providing interpretable expressions for effective relaxation rates, pole conditions, and perturbation responses. Within this setting, node-level quantities arise naturally once the dependence of global behaviour on local timing parameters is made explicit.

Another contribution of this work is its ability to resolve how local temporal perturbations reshape global dynamics. Because waiting-time kernels enter the operator in a node-specific manner, modifying the mean, variance, or tail behaviour of a single

distribution can accelerate or decelerate collective diffusion. This form of sensitivity does not arise in purely Markovian models, where all nodes share identical exponential clocks. The resulting dynamical importance measure quantifies how temporal heterogeneity alone independent of structural connectivity can influence global relaxation rates. The empirical analysis illustrates this point: node-specific renewal parameters uncover heterogeneity invisible to memoryless baselines and reveal how localized temporal features may contribute to functional bottlenecks or vulnerability patterns.

More broadly, these node-level diagnostics highlight the value of renewal-based approaches for analysing heterogeneous systems. By disentangling temporal and structural factors, the framework enables a detailed examination of how localized timing mechanisms shape emergent large-scale behaviour, with potential applications ranging from neurodegenerative spreading to transportation flows and communication networks.

Because our numerical experiments involve fitting model output to empirical measurements, it is important to clarify their intent. The aim is not to establish predictive superiority on unseen data, but to assess the explanatory capacity of renewal-driven diffusion relative to memoryless baselines. Existing Poisson-based or diagonal models often achieve only modest correlations (around $r \approx 0.6$) on comparable datasets, suggesting that their assumptions are too restrictive for the complexity of biological processes. In contrast, renewal-based parametrizations yield significantly higher agreement (e.g. $r > 0.79$ for the α-synuclein dataset examined here), demonstrating that incorporating realistic timing statistics meaningfully increases the expressive power of diffusion models. These gains are achieved using low-dimensional, physiologically interpretable parameter families constrained within biologically plausible ranges.

In summary, this work advances a general analytical framework for non-Markovian diffusion, clarifies how temporal heterogeneity shapes collective behaviour through spectral-temporal coupling, and demonstrates that renewal-based parametrizations can offer substantial explanatory improvements over classical Markovian models. Node-level influence measures emerge as natural consequences of this formulation, but the primary contribution lies in strengthening the methodological foundation for modelling and interpreting temporally complex diffusion processes on networks.

Data availability

The mouse-brain connectome diffusion dataset used in this study is available at https://github.com/ejcorn/connectome_diffusion. The exact input files used in our analyses, including the mouse-brain dataset and all other network datasets used in the experiments, are available at https://github.com/naivefrog0817-chengluo/temporal_diffusion.

Code availability

The code used in this study to generate the results and graphs is available at https://github.com/naivefrog0817-chengluo/temporal_diffusion. This repository contains the Python code and data used to reproduce the main analyses and numerical experiments.

References

[1] M. Jusup, P. Holme, K. Kanazawa, M. Takayasu, I. Romić, Z. Wang, S. Geček, T. Lipić, B. Podobnik, L. Wang, *et al.*, Social physics, Physics Reports **948**, 1 (2022).

[2] J. Weickenmeier, E. Kuhl, and A. Goriely, Multiphysics of prionlike diseases: Progression and atrophy, Physical review letters **121**, 158101 (2018).

[3] D. Witthaut, F. Hellmann, J. Kurths, S. Kettemann, H. Meyer-Ortmanns, and M. Timme, Collective nonlinear dynamics and self-organization in decentralized power grids, Reviews of modern physics **94**, 015005 (2022).

[4] N. Masuda, M. A. Porter, and R. Lambiotte, Random walks and diffusion on networks, Physics reports **716**, 1 (2017).

[5] A. R. Benson, D. F. Gleich, and J. Leskovec, Higher-order organization of complex networks, Science **353**, 163 (2016).

[6] C. Bick, E. Gross, H. A. Harrington, and M. T. Schaub, What are higher-order networks?, SIAM review **65**, 686 (2023).

[7] F. Battiston, E. Amico, A. Barrat, G. Bianconi, G. Ferraz de Arruda, B. Franceschiello, I. Iacopini, S. Kéfi, V. Latora, Y. Moreno, *et al.*, The physics of higher-order interactions in complex systems, Nature physics **17**, 1093 (2021).

[8] Y. Zhang, P. S. Skardal, F. Battiston, G. Petri, and M. Lucas, Deeper but smaller: Higher-order interactions increase linear stability but shrink basins, Science Advances **10**, eado8049 (2024).

[9] J.-C. Delvenne, R. Lambiotte, and L. E. Rocha, Diffusion on networked systems is a question of time or structure, Nature communications **6**, 7366 (2015).

[10] M. Rosvall, A. V. Esquivel, A. Lancichinetti, J. D. West, and R. Lambiotte, Memory in network flows and its effects on spreading dynamics and community detection, Nature communications **5**, 4630 (2014).

[11] L. Backstrom and J. Leskovec, Supervised random walks: predicting and recommending links in social networks, in *Proceedings of the fourth ACM international conference on Web search and data mining* (2011) pp. 635–644.

[12] R. Lambiotte, M. Rosvall, and I. Scholtes, From networks to optimal higher-order models of complex systems, Nature physics **15**, 313 (2019).

[13] P. Holme and J. Saramäki, *Temporal network theory*, Vol. 2 (Springer, 2019).

[14] E. W. Montroll and G. H. Weiss, Random walks on lattices. ii, Journal of Mathematical Physics **6**, 167 (1965).

[15] R. Balescu, *Statistical Dynamics: Matter Out of Equilibrium* (World Scientific, Singapore, 1997).

[16] D. Chruściński, Dynamical maps beyond markovian regime, Physics Reports **992**, 1 (2022).

[17] M. Feng, S.-M. Cai, M. Tang, and Y.-C. Lai, Equivalence and its invalidation between non-markovian and markovian spreading dynamics on complex networks, Nature communications **10**, 3748 (2019).

[18] J. Goutsias and G. Jenkinson, Markovian dynamics on complex reaction networks, Physics reports **529**, 199 (2013).

[19] J. G. Restrepo, E. Ott, and B. R. Hunt, Characterizing the dynamical importance of network nodes and links, Physical review letters **97**, 094102 (2006).

[20] E. Young and M. A. Porter, Dynamical importance and network perturbations, Physical Review E **110**, 064304 (2024).

[21] A. Raj, A. Kuceyeski, and M. Weiner, A network diffusion model of disease progression in dementia, Neuron **73**, 1204 (2012).

[22] M. X. Henderson, E. J. Cornblath, A. Darwich, B. Zhang, H. Brown, R. J. Gathagan, R. M. Sandler, D. S. Bassett, J. Q. Trojanowski, and V. M. Lee, Spread of α-synuclein pathology through the brain connectome is modulated by selective vulnerability and predicted by network analysis, Nature neuroscience **22**, 1248 (2019).

[23] E. J. Cornblath, H. L. Li, L. Changolkar, B. Zhang, H. J. Brown, R. J. Gathagan, M. F. Olufemi, J. Q. Trojanowski, D. S. Bassett, V. M. Lee, *et al.*, Computational modeling of tau pathology spread reveals patterns of regional vulnerability and the impact of a genetic risk factor, Science Advances **7**, eabg6677 (2021).

[24] W. Chen, Y. Wang, and S. Yang, Efficient influence maximization in social networks, in *Proceedings of the 15th ACM SIGKDD international conference on Knowledge discovery and data mining* (2009) pp. 199–208.

[25] R. Pastor-Satorras and A. Vespignani, Immunization of complex networks, Physical review E **65**, 036104 (2002).

[26] M. A. Porter and J. P. Gleeson, Dynamical systems on networks, Frontiers in Applied Dynamical Systems: Reviews and Tutorials **4**, 29 (2016).

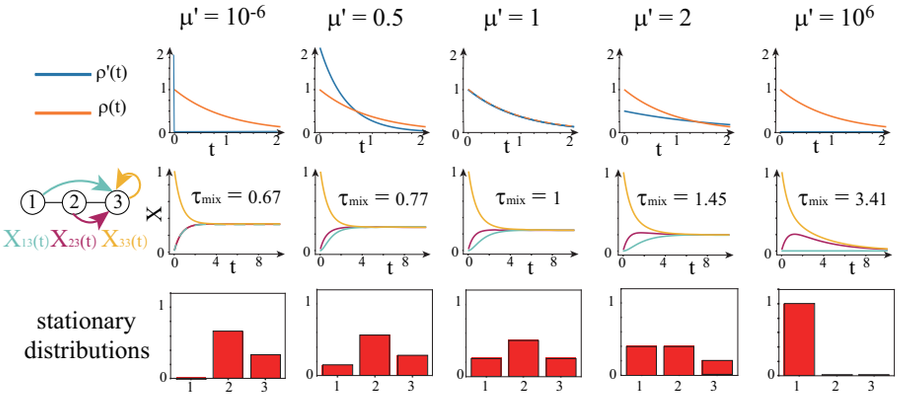

Acknowledgements

The computations in this research were performed using the CFFF platform of Fudan University. During the preparation of this manuscript, the authors used ChatGPT to assist in language polishing. The authors carefully reviewed and revised the output accordingly and take full responsibility for the content of the final manuscript. The authors would like to thank Alexander Grin (from Interdisciplinary Research Centre for Complex Systems), Jiachen Ye, Yong Zou, and Gang Yan for comments on the manuscript.

Funding

C.L. and P.J. acknowledge support from Brain Science and Brain-like Intelligence Technology - National Science and Technology Major Project (2021ZD0204500, 2021ZD0204504), and National Natural Science Foundation of China (62576108). R.L. acknowledges support from the EPSRC grants EP/V013068/1, EP/V03474X/1 and EP/Y028872/1.

Author contributions

P.J. conceived the project. C.L., P.J. and R.L. designed the experiments. C.L. performed the experiments and analyzed the data. C.L. and P.J. discussed the results. C.L. wrote the first draft. P.J. and R.L. participated in editing the manuscript. C.L. and P.J. contributed to the final manuscript. C.L. and P.J. answered the referees.

Competing interests

The authors declare no competing interests.

Figure Legends

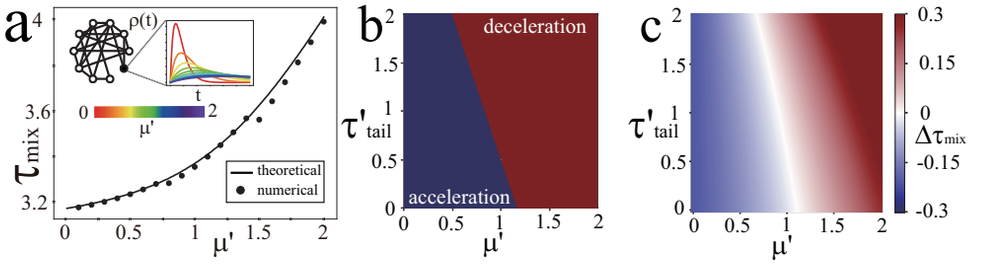
a
b
c
ρ(t)
t
μ'
τmix
theoretical
numerical
deceleration
acceleration
τ'tail
Δτmix

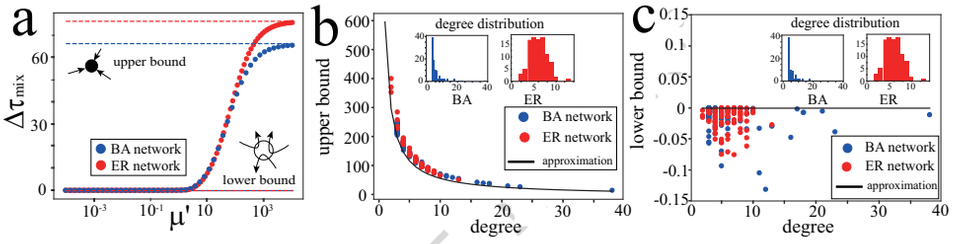
a
b
c
upper bound
lower bound
BA network
ER network
Δτmix
μ'
degree distribution
BA
ER
approximation
upper bound
lower bound
degree

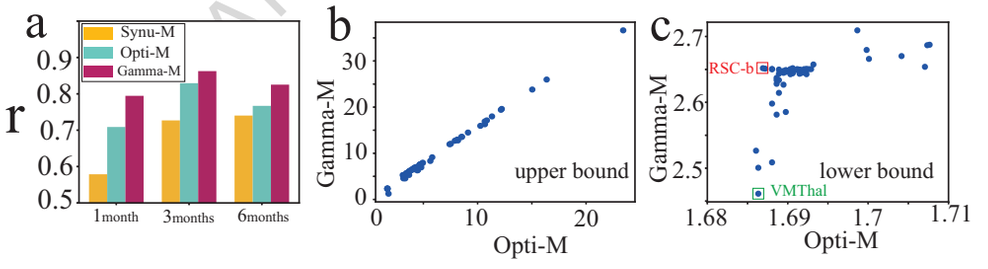
a
b
c
r
Synu-M
Opti-M
Gamma-M
1month
3months
6months
upper bound
lower bound
Opti-M
RSC-b
VMThal

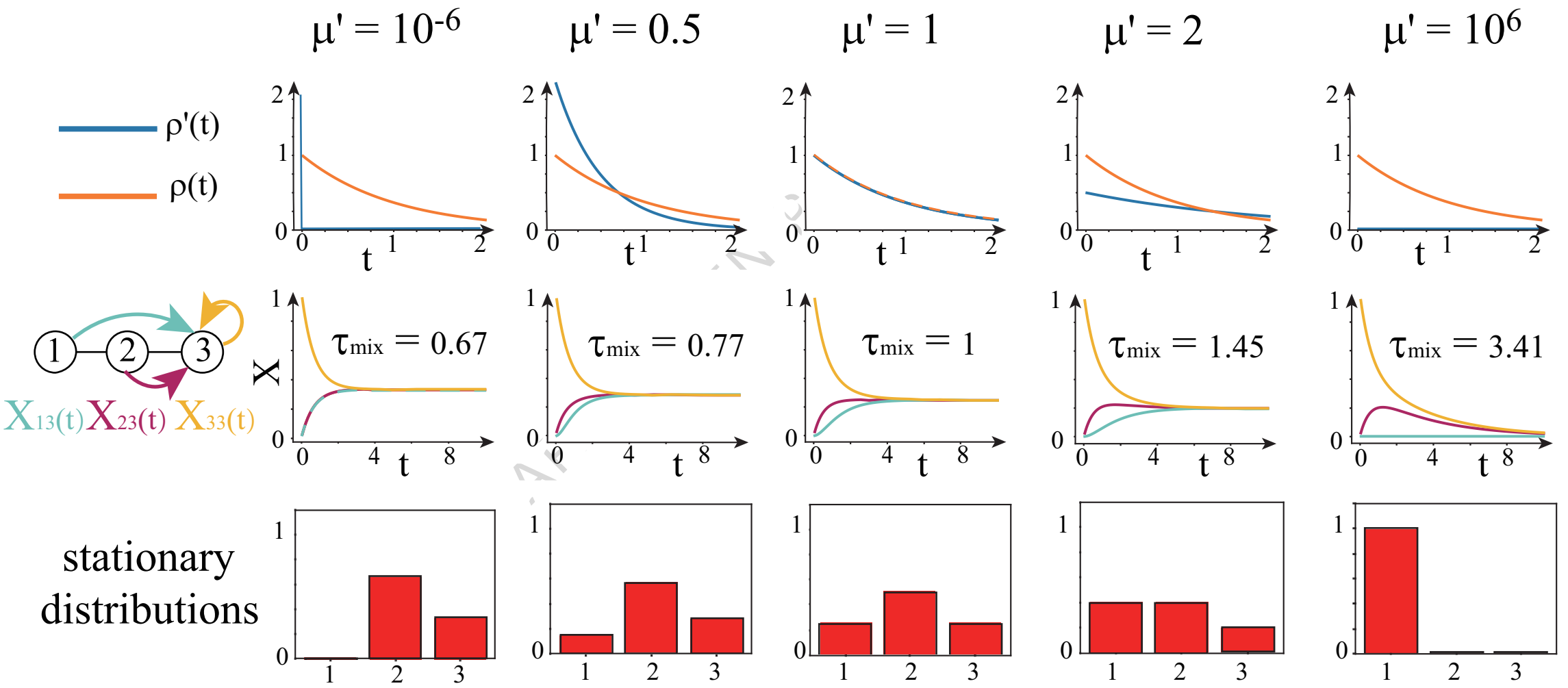
μ' = 10-6
μ' = 0.5
μ' = 1
μ' = 2
μ' = 10^6
ρ'(t)
ρ(t)
t
1
2
3
X13(t) X23(t) X33(t)
X
τmix = 0.67
τmix = 0.77
τmix = 1
τmix = 1.45
τmix = 3.41
stationary distributions

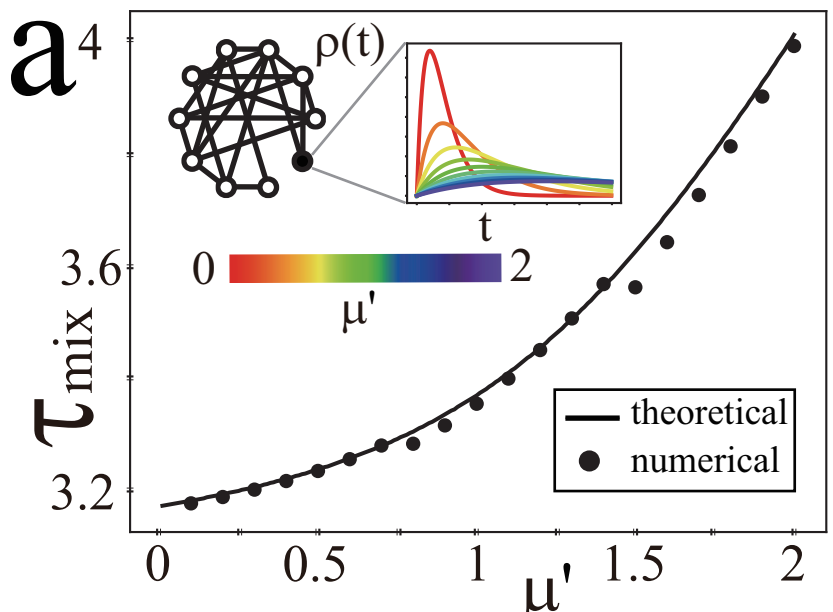
a
ρ(t)
t
0
2
μ'
τmix
3.6
3.2
theoretical
numerical
0
0.5
1
1.5
2
μ'

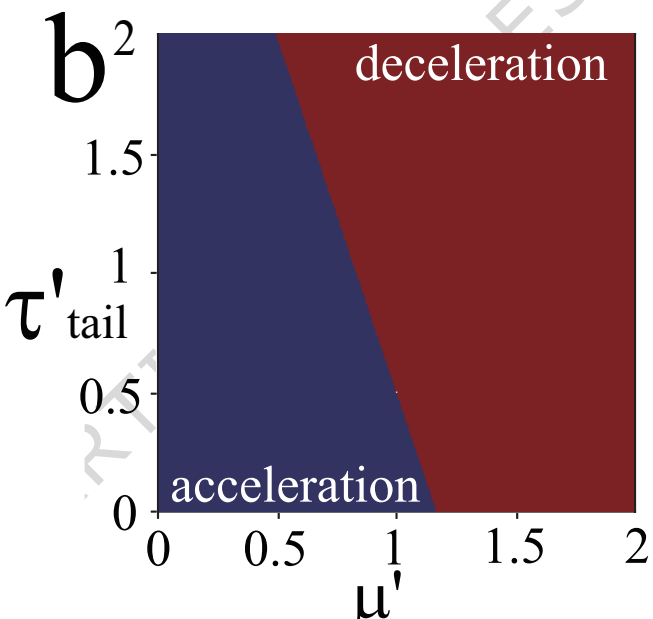
b
deceleration
acceleration
τ'tail
2
1.5
1
0.5
0
0
0.5
1
1.5
2
μ'

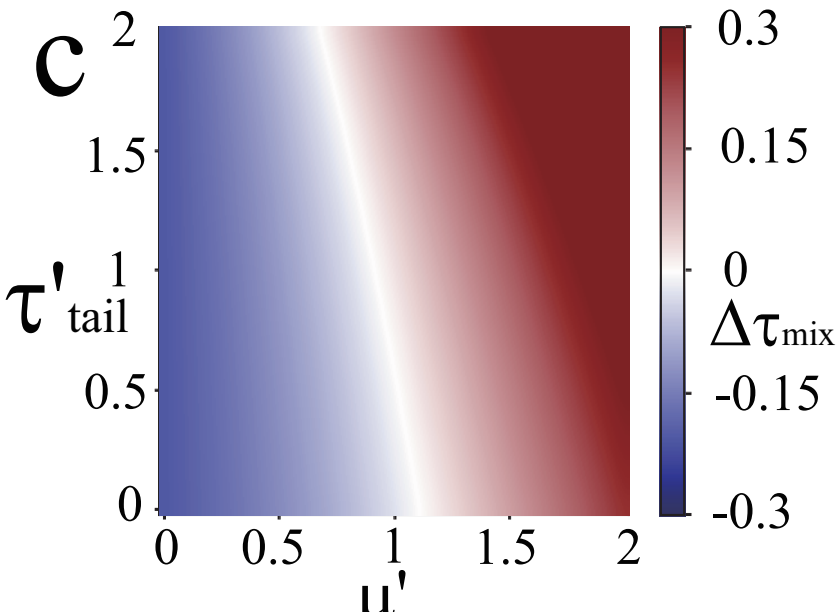
c
τ'tail
2
1.5
1
0.5
0
0
0.5
1
1.5
2
μ'
0.3
0.15
0
-0.15
-0.3
Δτmix

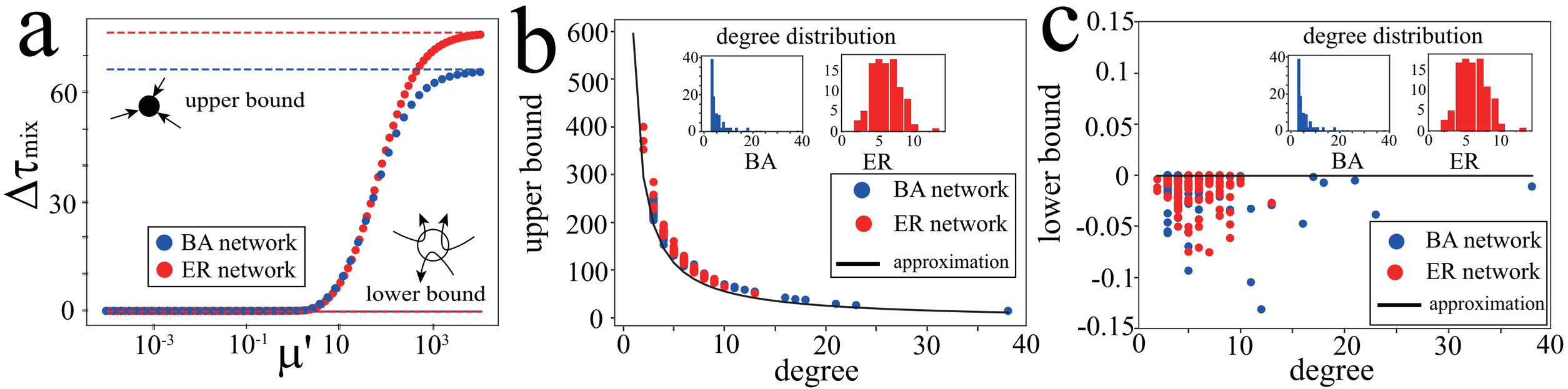
a
$\Delta\tau_{mix}$
60
30
0
upper bound
lower bound
BA network
ER network
10^{-3}
10^{-1}
μ'
10
10^{3}
b
upper bound
600
500
400
300
200
100
0
degree distribution
40
20
0
0
20
40
BA
15
10
5
0
0
5
10
ER
BA network
ER network
approximation
0
10
20
30
40
degree
c
lower bound
0.15
0.1
0.05
0
-0.05
-0.1
-0.15
degree distribution
BA
ER
BA network
ER network
approximation
0
10
20
30
40
degree